Microporous and Mesoporous Materials 124 (2009) 169–178

Contents lists available at ScienceDirect

Microporous and Mesoporous Materials

journal homepage: www.elsevier.com/locate/micromeso

Highly ordered mesoporous titania–zirconia photocatalyst for applications in degradation of rhodamine-B and hydrogen evolution

Quan Yuan, Yang Liu, Le-Le Li, Zhen-Xing Li, Chen-Jie Fang, Wen-Tao Duan, Xing-Guo Li, Chun-Hua Yan *

Beijing National Laboratory for Molecular Sciences, State Key Laboratory of Rare Earth Materials Chemistry and Applications, PKU-HKU Joint Laboratory in Rare Earth Materials and Bioinorganic Chemistry, Peking University, Haidian, Beijing 100871, China

ARTICLE INFO

Article history:
Received 25 August 2008
Received in revised form 28 December 2008
Accepted 2 May 2009
Available online 9 May 2009

Keywords:
Mesoporous structure
Titania–zirconia composites
Photocatalysis
Rhodamine-B degradation
Hydrogen evolution

ABSTRACT

We report a facile synthesis of highly ordered mesoporous titania–zirconia composites with broad Ti/Zr ratios via an evaporation-induced self assembly (EISA) process. Amphiphilic poly(alkylene oxide) block copolymers, P123 and F127, serve as structure-directing agents (SDAs). By adjusting initial molar ratios of copolymer to metal precursors, titania–zirconia nanocomposites with controlled texture and composition are obtained in a wide range from 10 to 90 mol% TiO_2. Small-angle X-ray diffraction (SAXRD) and transmission electron microscopy (TEM) measurements reveal the two-dimensional (2D) hexagonal mesostructure (*p6mm*) with large-domain regularity. These mesostructured composites possess large surface areas and pore volumes, narrow pore size distributions, and abundant surface Lewis acid sites, resulting in unique photocatalytic activities for degradation of rhodamine-B and hydrogen evolution in methanol aqueous solution. Their good photocatalytic abilities are ascribed to the cooperative effect of the porosity and crystallinity.

1. Introduction

Due to its unique optical and electronic properties and nontoxic nature, titania possess various utilities in areas of energy conversion, catalysis and photocatalysis, coatings, and chemical sensors [1]. It crystallizes in three structure types: rutile, anatase, and brookite, with large band gaps 3.0 eV for rutile form and 3.2 eV for antase form [2]. A photon with energy equivalent to or greater than the band gap generates an electron–hole pair on the TiO_2 surface, which cause reduction and oxidation reactions [3], promising the use of TiO_2 as a good photocatalyst. For example, it was the first material as a photochemical water-splitting catalyst [4,5]. However, pure TiO_2 materials usually have relatively low quantum efficiency, which restricts its extended applications in catalysis. Combination with another metal oxide is presently the most practicable approach for property tuning [6,7]. These combined metal oxide materials bring forth new reactivity properties and enhanced activity due to structural and electronic modifications induced by the dopant [8,9]. A great deal of $Ti_{1-x}M_xO_2$ such as TiO_2–SiO_2, TiO_2–ZrO_2, or TiO_2–Al_2O_3 [10–14] has been reported, among which the TiO_2–ZrO_2 mixed metal oxide is most promising as photocatalysts [15–17]. TiO_2–ZrO_2 binary oxides with multiphasic composition exhibit an increase in the photocatalytic degradation rate of different pollutants in both gas and aqueous solutions [17,18]. Fu et al. [19] and Yu et al. [20] have shown that TiO_2–ZrO_2 binary metal oxides exhibit higher photocatalytic activity than pure TiO_2, possibly due to the increase in surface area with respect to TiO_2 at the same calcination temperature, the inhibition from rutile formation, the increase in surface acidity (i.e. stronger surface hydroxyl groups), or the creation of active defects on the surface.

Great efforts have been paid to reveal the relationship between the morphology and properties of nanomaterials [21–24]. Morphological control of materials involves variety of aspects, including the regulation of shape, size, structure, pore size, connectivity, colloidal dimensions, etc. Diverse morphologies such as particles, fibers, films, and porous structures result in different properties for various applications [18]. Since the discovery of MCM-41 in 1992 [25], increasing attention has been focused on the design and synthesis of silica and non-silica mesoporous materials for their potential application in catalysis, energy, optics, electronics, biology, and others [26]. Numerous synthesis strategies are reported, among which the evaporation-induced self-assembly (EISA), pioneered by Brinker et al. [27,28] and adapted by Stucky and coworkers [29], allows for tuning of inorganic hydrolysis-condensation rate. This method has been used to prepare highly ordered mesoporous oxide thin films with controlled symmetry by adjusting precursor composition and relative humidity [30], since slow co-assembly of the inorganic network around the liquid crystalline template permits the formation of a well-defined mesoporous structure. Over the past two decades, great interests have been

* Corresponding author. Tel./fax: +86 10 6275 4179.
E-mail address: yan@pku.edu.cn (C.-H. Yan).

1387-1811/$ - see front matter © 2009 Elsevier Inc. All rights reserved.
doi:10.1016/j.micromeso.2009.05.006

concentrated on the achievement of ordered mesoporous TiO_2 with high crystallinity frameworks and high thermal stability [31–37]. Moreover, the synthesis of mesoporous zirconia with hexagonal and cubic structures was first realized by Stucky's group employing triblock copolymers as templates [29]. However, for multiple-metal oxides, specific chemistry for each metal species, especially different hydrolysis rate for different metal precursors, makes the control of the hydrolysis-condensation process difficult [38]. To our knowledge, it is still a challenge for controlled synthesis of the multiple-metal oxides with ordered mesoporous structures through the EISA process.

Compared to pure TiO_2, TiO_2–ZrO_2 composites have tunable composition, abundant phases and more attractive photocatalysis properties. Numerous efforts have been devoted to synthesize TiO_2–ZrO_2 with different morphologies [39–41]. It is postulated that ordered mesoporous TiO_2–ZrO_2 composites with wide Ti/Zr ratios will possess specific photocatalytic properties due to the large surface area, unsaturated titanium(IV) sites, oxygen vacancies existing on the surface, and high thermal stability. As for synthesis, as mentioned above, ordered mesoporous TiO_2 with crystalline walls are easily achieved, however, ordered mesostructured TiO_2–ZrO_2 has been rarely reported. Caruso et al. reported porous Titania/Zirconia with pore of 1 μm using polymer gel template [18] and proved these materials had good photocatalytic activities for decomposition of organic molecules. Liu et al. obtained mesoporous TiO_2–ZrO_2 composites utilizing triblock copolymer as template [42] but their results only showed disordered mesostructures. To the best of our knowledge, highly ordered mesoporous multi-metal composites such as TiO_2–ZrO_2 composites with varied Ti/Zr ratios have not been reported. Although some specific conclusions have been drawn from above studies on photocatalytic properties of TiO_2 with ordered mesoporous structures, there is a lack of systematic synthesis and detailed measurements of photocatalytic properties of ordered mesoporous TiO_2–ZrO_2 composites. Therefore, it is necessary to study the synthesis and physical properties of ordered mesoporous TiO_2–ZrO_2 composites.

Herein, an efficient and reproducible approach to fabricate ordered mesoporous titania–zirconia composites with variable ratios through EISA process by using amphiphilic triblock copolymer F127 and P123 as structure-directing agents (SDAs) is reported. To reveal the formation mechanism of ordered mesostructures, the Ti/Zr ratio, quantity of block copolymers, relative humidity of the surrounding atmosphere, and evaporation temperature have been investigated in detail. To observe the structural evolution of the mesostructures with different Ti/Zr ratios, the measurements of X-ray diffraction (XRD) and transmission electron microscopy (TEM) were employed. Within tunable Ti/Zr ratios, these TiO_2–ZrO_2 nanocomposites possess highly ordered two-dimensional (2D) hexagonal mesostructure. Moreover, these mesoporous TiO_2–ZrO_2 nanocomposites exhibit high surface areas, narrow pore size distributions, and abundant of surface Lewis acid sites, resulting in unique photocatalytic activity in degradation of rhodamine-B (RhB) and hydrogen evolution.

2. Experimental

2.1. Materials

Pluronic F127 (M_{av} = 12600, $EO_{106}PO_{70}EO_{106}$) and Pluronic P123 (M_{av} = 5800, $EO_{20}PO_{70}EO_{20}$) were purchased from Aldrich and Sigma–Aldrich Chemical Inc. Zirconium oxide chloride ($ZrOCl_2{\cdot}8H_2O$), tetrabutyl titanate ($[CH_3(CH_2)_3O]_4Ti$), and RhB ($C_{28}H_{31}ClN_2O_3$) were purchased from Beijing Chemical Reagent Company. RhB was dissolved in deionzed water to form 1×10^{-5} M aqueous solution. P25 powder was supplied by Degussa Corp. All chemicals were used as received.

2.2. Synthesis of Mesoporous TiO_2–ZrO_2

0.7–1.0 g Pluronic F127 or 0.5–1.0 g Pluronic P123 was dissolved in 10 mL of ethanol at room temperature. Then quantitative $[CH_3(CH_2)_3O]_4Ti$ and $ZrOCl_2{\cdot}8H_2O$ were added (total amount of Ti plus Zr is 5 mmol) into the above solution with vigorous stirring. The composition of Ti/Zr/F127/EtOH (molar ratio) was varied in the range of (0.5–4.5)/(4.5–0.5)/(0.05–0.08)/170. The mixture was covered with polyethylene film. After stirring for at least 2 h at room temperature, the homogeneous sol was transferred to an oven and underwent solvent evaporation. After two days of aging under desired temperature and humidity (temperature: 40 °C, relative humidity (RH): 50%), the gel product was dried in another oven at 100 °C for 1 day. Calcination was carried out by slowly increasing temperature from room temperature to 400 °C (1 °C min^{-1} ramping rate) and heating at 400 °C for 4 h in air. High temperature treatment was carried out in air for 1 h with a temperature ramp of 10 °C min^{-1}.

2.3. Degradation of RhB

The meso-TiO_2–ZrO_2 samples were dispersed into 150 mL RhB aqueous solution (1×10^{-5} mol L^{-1}) and the resulting solution was stirred in dark for 2 h to equilibrate the adsorption–desorption of RhB on the sample surface. Five-hundred Watt high pressure mercury lamp (center wavelength is 365 nm) was used as an irradiation source. At given time intervals, the supernate was analyzed by recording the variations of the absorption band maximum (554 nm) on a Shimadzu UV-3100 spectrometer. For comparison, all the samples tested for the activity were weighted exactly same (100 mg).

2.4. Hydrogen evolution

The photocatalytic hydrogen generation was carried out in a Pyrex glass container with a volume of 320 mL. Five-hundred Watt high pressure mercury lamp (center wavelength is 365 nm) equipped with cooling water was used as an irradiation source, which was placed in a fixed distance from photocatalytic reactor. The intensity of irradiation is 5.5 mW cm^{-1}. The photocatalytic reaction of water splitting was performed in 60 mL solution (35 mL distilled water and 25 mL methanol as sacrifice agent). 0.06 g photocatalyst was added into the solution. Before mercury lamp was turned on, the suspension was thoroughly degassed through bubbling argon gas into the system for 30 min to purge out dissolved oxygen. After the lamp was turned on, the solution was stirred. In order to keep reaction temperature constant at 25 °C, the photocatalytic reaction system was equipped with an electric fan. The evolved hydrogen was measured by gas chromatography equipped with TCD detector and molecular sieve 5 A column. Carrier gas was argon.

2.5. Characterization

Powder X-ray diffraction (PXRD) patterns were recorded on a Rigaku D_{MAX}-2000 diffractometer (Japan) using Cu Kα radiation (λ = 1.5406 Å). Transmission electronic microscopy (TEM) and energy dispersive X-ray analysis (EDAX) were taken on a Hitachi H-9000 NAR transmission electron microscope (Japan) under a working voltage of 300 kV. The nitrogen adsorption and desorption isotherms at 78.3 K were measured using an ASAP 2010 analyzer (Micromeritics Co. Ltd., USA). The Brunauer–Emmett–Teller (BET) method was utilized to calculate the specific surface areas (S_{BET})

using adsorption data in a relative pressure ranging from 0.04 to 0.2. Using the Barrett–Joyner–Halenda (BJH) model, the pore volumes and pore size distributions were derived from the adsorption branches of the isotherms. FTIR spectra were recorded on a Nicolet Magna-IR 750 spectrometer equipped with a Nic-Plan Microscope (USA). Weight changes of the products were carried out on a Thermal Analysis SDT Q600 analyzer (USA) from 25 °C to 1000 °C under air atmosphere with a heating rate of 10 °C min^{-1}. The UV–Vis absorbance spectra of RhB were recorded on a Shimadzu UV-3100 spectrophotometer (Japan) with a quartz cell (10 mm path length) and deionized water as a blank. X-ray photoelectron spectroscopy (XPS) measurements were carried out in an ion-pumped chamber (evacuated to 2×10^{-9} Torr) of an Axis Ultra (UK) spectrometer equipped with a focused monochromatized X-ray source (Al Kα, h = 1486.6 eV) at a power of 225 W. A hemispherical analyzer collected the photoelectrons at an angle of 90° from the surface. The binding energy (*BE*) for the samples was calibrated by setting the measured *BE* of C 1*s* to 284.6 eV.

3. Results and discussion

Ordered mesoporous $50TiO_2$–$50ZrO_2$ (denoted as meso-50TZ) was synthesized with a reactant molar ratio of F127/$[CH_3(CH_2)_3$-$O]_4$Ti/ZrOCl·$8H_2O$/ethanol = 0.056/0.25/0.25/170, and well-ordered mesoporous structure was obtained. This determination comes from the analysis of the small-angle X-ray diffraction (XRD) patterns (Fig. 1a), showing a prominent reflection peak at 0.98° along with a broad low intensity peak around ca. 1.8°, which, according to the TEM observation, matches well with the characteristic (1 0 0), (1 1 0), and (2 0 0) reflections attributed to *p6mm* hexagonal symmetry. When calcined at 600 °C, the peak at low angle range is retained with a little shift to high angle, suggesting the decrease of the *d* with the increase of temperature. No reflection peak is detected in the small-angle XRD patterns when the calcinations temperature increases to 800 °C and 900 °C, demonstrating the collapse of the mesoporous structure. Wide-angle XRD patterns (Fig. 1b) display only broad peaks for the samples calcined at 400 °C, demonstrating that the pore walls of meso-50TZ are amorphous. After calcined at 800 °C, the frameworks crystallize to $ZrTiO_4$ (JCPDS Card No. 34–0415). It is obvious that crystallization of the frameworks leads to collapse of mesoporous structure due to the instantaneous phase transition and rapid nanocrystallite growth.

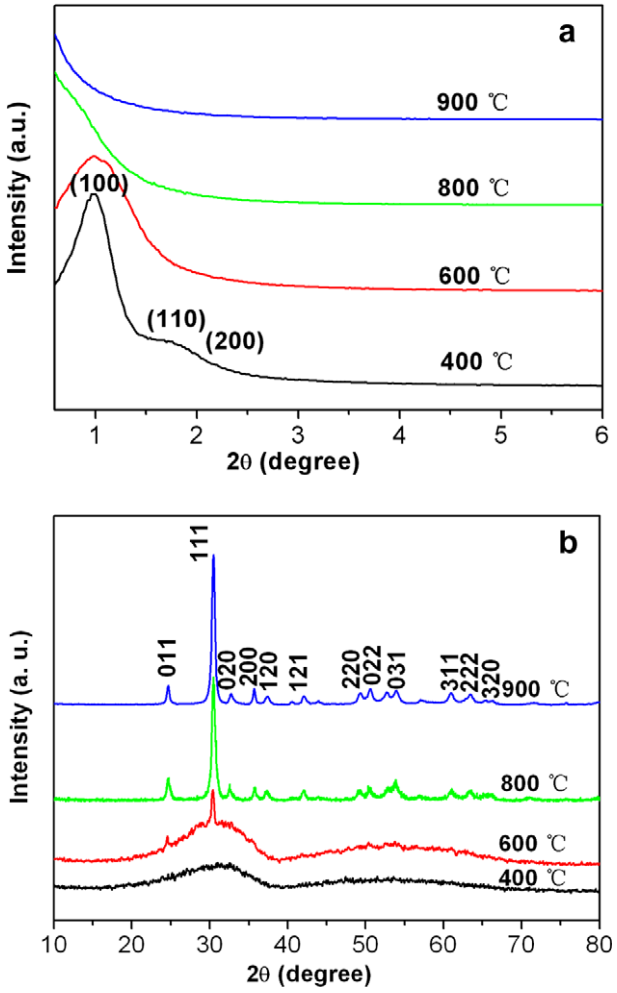

Fig. 1. (a) Small- and (b) wide-angle XRD patterns of meso-50TZ calcined at different temperatures.

TEM images viewed along the [0 0 1] and [1 1 0] directions (Fig. 2a and b) further confirm that meso-50TZ calcined at 400 °C has a highly ordered 2D hexagonal regularity. As the calcination temperature increases to 600 °C, the regularity of mesoporous structure remains and large domains of highly ordered cylindrical pore channels with the 2D hexagonal symmetry are still observed in a large domain from the TEM images (Fig. 2c and d). The cell parameter estimated from the TEM images is approximately 9 nm for 400 °C product and 8 nm for 600 °C product, which is in agreement with the value calculated from the small-angle XRD data.

The nitrogen sorption analysis yields typical IV curves with type H1 hysteresis loops for both products calcined at 400 °C and 600 °C (Fig. 3a). The high BET surface areas of 186 and 170 $m^2 g^{-1}$ is obtained for the products of 400 °C and 600 °C, respectively. Nitrogen sorption measurements show that the pore size of meso-50TZ composites decreases with calcinations temperature (Fig. 3b), possessing narrow mesopore size distributions at a mean size of 4.6 and 4.1 nm for the products calcined at 400 °C and 600 °C, respectively. After calcined at higher temperature, the specific surface area decreases quickly. The BET surface areas of 37 $m^2 g^{-1}$ and 18 $m^2 g^{-1}$ are obtained for the products of 800 °C and 900 °C, respectively, which are much lower than that calcined at 400 °C and 600 °C, and these results prove breakdown of mesostructures during high temperature treatment. The pore volumes vary from 0.29 $m^3 g^{-1}$ to 0.19 $m^3 g^{-1}$ when calcined at different temperatures. The high surface area and uniform pore structure should make it more popular in catalysis.

Thermogravimetric-differential thermal analysis (TG-DTA) profiles of the as-synthesized meso-50TZ sample under air atmosphere are given in Fig. 4. The major weight-loss stage is observed below 400 °C with a weight loss of about 60 wt.%. This weight loss is attributed to the decomposition of amphiphilic triblock copolymer F127 combined with the removal of physically absorbed water and the dehydration of zirconium–titanium hydroxide. A remarkable exothermic effect centered at 300 °C is shown in DTA curve, which mainly relates to the combination of the decomposition of F127 and the dehydration of zirconium–titanium hydroxide. The as-synthesized sample also shows an exothermic effect centered at 720 °C due to the crystallization of pore walls to $ZrTiO_4$, leading to the collapse of the mesostructure.

To test the surface acidity of meso-50TZ calcined at different temperautre, FTIR study on pyridine adsorption are performed. As shown in Fig. 5, the bands at 1608 and 1447 cm^{-1} are evidence of electron-acceptor centers on material surface, with which pyridine forms coordination bonds corresponding to the ν_{8a} and ν_{19b} modes of the ring-breathing vibrations ν(CCN) of pyridine, respectively. Parfitt et al. [43] assigned these bands to Lewis acid sites of Type I, which strongly adsorbed pyridine. The amount of absorbed

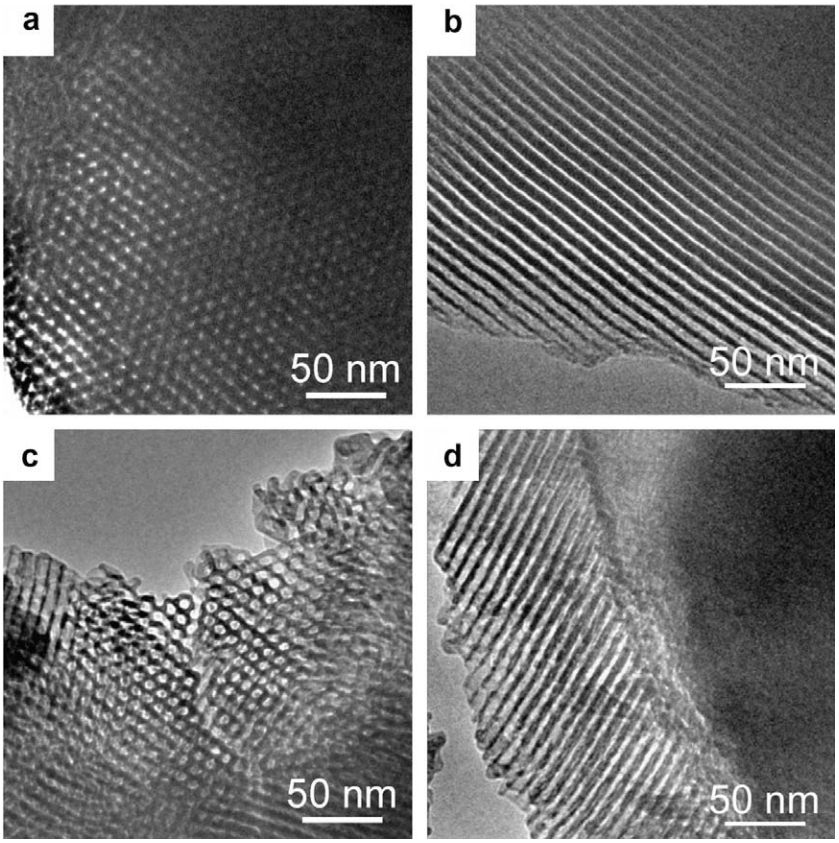

Fig. 2. TEM images (a) and (b) of meso-50TZ calcined at 400 °C viewed along [0 0 1] and [1 1 0] orientation; (c) and (d) of meso-50TZ calcined at 600 °C viewed along [0 0 1] and [1 1 0] orientation.

pyridine on Lewis acid sites is estimated by the absorbance of the band (ν_{19b} mode) around 1447 cm^{-1}. The numbers of Lewis acid sites calculated for meso-50TZ calcined at different temperatures are large and decrease gradually with the calcined temperatures elevated (Table S1 in the Supporting Information).

Highly ordered mesoporous titania–zirconia composites can be synthesized via an EISA process in ethanol media using $[CH_3(CH_2)_3O]_4Ti$ and $ZrOCl_2{\cdot}8H_2O$ as titanium and zirconium sources, and F127 or P123 as template. The formation of mesostructured TiO_2–ZrO_2 nanocomposites undergoes a cooperative self-assembly process [44] of titanate oligomers hydrolyzed from $[CH_3(CH_2)_3O]_4Ti$, zirconia oligomers from $ZrOCl_2{\cdot}8H_2O$, and amphiphilic triblock copolymer. In most cases with EISA strategy to fabricate mesoporous metal oxide, acids are often necessary to slow down the hydrolysis-condensation rate of the metal precursors [45]. Herein, no extra acid is added for adjusting the hydrolysis rates of different metal species, however, the hydrolysis of zirconium oxychloride and titania alkoxide follows a self-adjusted process, resulting in a synchronized condensation–polymerization process of these two metal species. The final mesostructured composites have a uniform and homogeneous framework with well-dispersed titanate and zirconate components, in which both oligomers cross-link together and construct the mesostructured frameworks. In addition, the temperature and relative humidity (RH) of the surrounding atmosphere play an important role in synchronizing the assembly of the titanate and zirconate oligomers during the EISA process. After finely tuning this factor, 40 °C and 50% RH is the optimized condition and is adopted in the present work. It proves that this procedure is controllable and repeatable for the organization of highly ordered composite mesostructures within a wide range of Ti/Zr ratios.

Varying the Ti/Zr ratios, a series of mesoporous TiO_2–ZrO_2 are obtained by adjusting the quantities of SDAs, which is confirmed by small-angle XRD patterns shown in Fig. 6. The intensity and width of the peak vary with the Ti/Zr ratio, indicating that the mesostructure is strongly affected by the composition. The mesoporous 10 TiO_2–$90ZrO_2$ (denoted as meso-10TZ) sample shows three well-resolved diffraction peaks indexed as the (1 0 0), (1 1 0), and (2 0 0) reflections, respectively, suggesting a typical 2D hexagonal mesostructure belonging to *p6mm* hexagonal symmetry. $20TiO_2$–$80ZrO_2$ (denoted as meso-20TZ), $40TiO_2$–$60ZrO_2$ (denoted as meso-40TZ), and $60TiO_2$–$40ZrO_2$ (denoted as meso-60TZ) samples all possess 2D hexagonal mesostructures according to the small-angle XRD patterns. When Ti increases to 80 mol% (denoted as meso-80TZ) and 90 mol% (denoted as meso-90TZ), the diffraction peak of (1 0 0) becomes broad and no small diffraction peak is observed, indicating a short range ordered mesostructure. Wide-angle XRD analysis gave information about the crystal phase of these series of mesoporous TiO_2–ZrO_2 composites with different Ti/Zr ratios (Fig. 7a). The meso-90TZ network exhibits diffraction peaks attributed to anatase titania ((JCPDS Card No. 71–1169). A further increase of the zirconia content inhibits crystallization, as no crystallinity is detected with wide-angle XRD in the binary metal oxide samples meso-80TZ and meso-60TZ, demonstrating a homogeneous mixing of the Ti and Zr components in both the materials. The wide-angle XRD patterns from the samples containing zirconia as the major component, meso-40TZ to meso-10TZ, are assigned to tetragonal phase of zirconia (JCPDS Card No. 02–0733). After 600 °C treatment, the mesostructures of meso-10TZ, 20TZ, and 40TZ samples are sustained with a little shrinkage (Fig. 7b) while those of meso-60TZ, 80TZ, 90TZ samples collapse. Wide-angle XRD patterns show that 10TZ and 20TZ treated at 600 °C

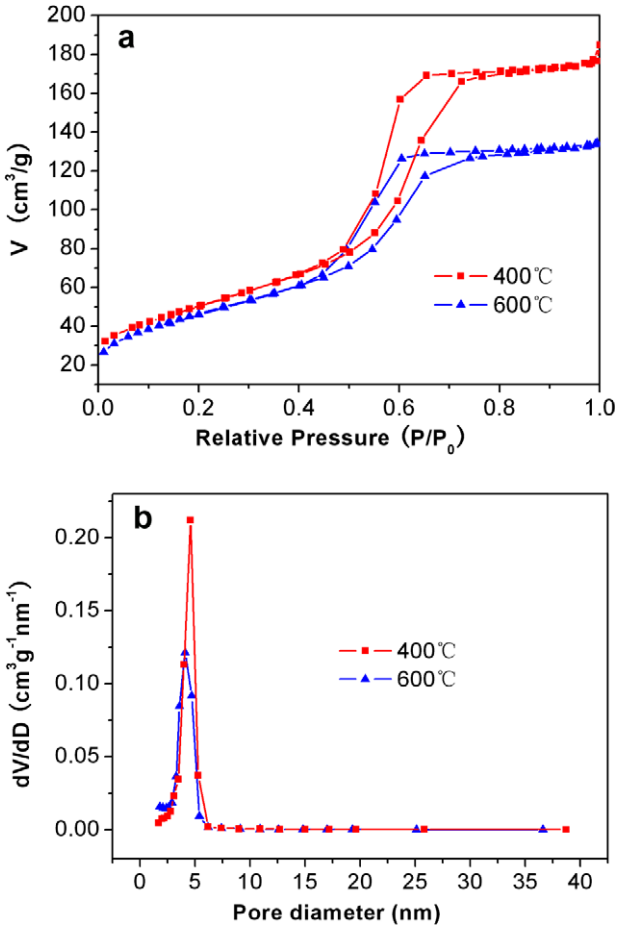

Fig. 3. (a) Nitrogen adsorption–desorption isotherms and (b) pore size distribution curves (deduced from the desorption branches) of meso-50TZ calcined at different temperatures.

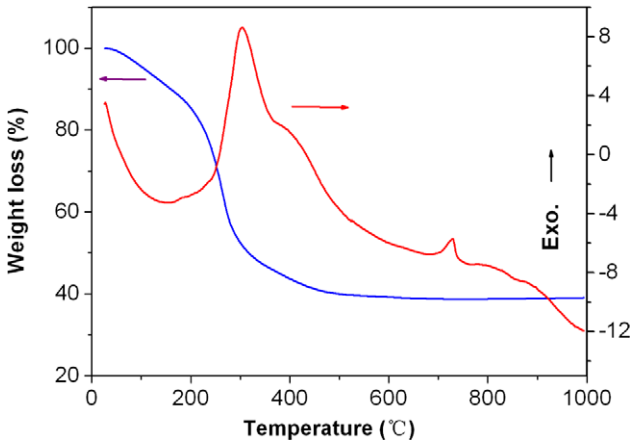

Fig. 4. TG-DTA profiles for the as-synthesized meso-50TZ.

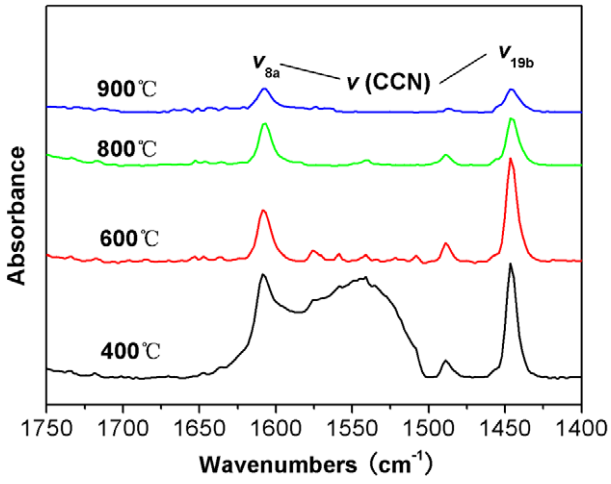

Fig. 5. FTIR spectra of pyridine adsorption for Al-1 at the deposition temperature of 200 °C.

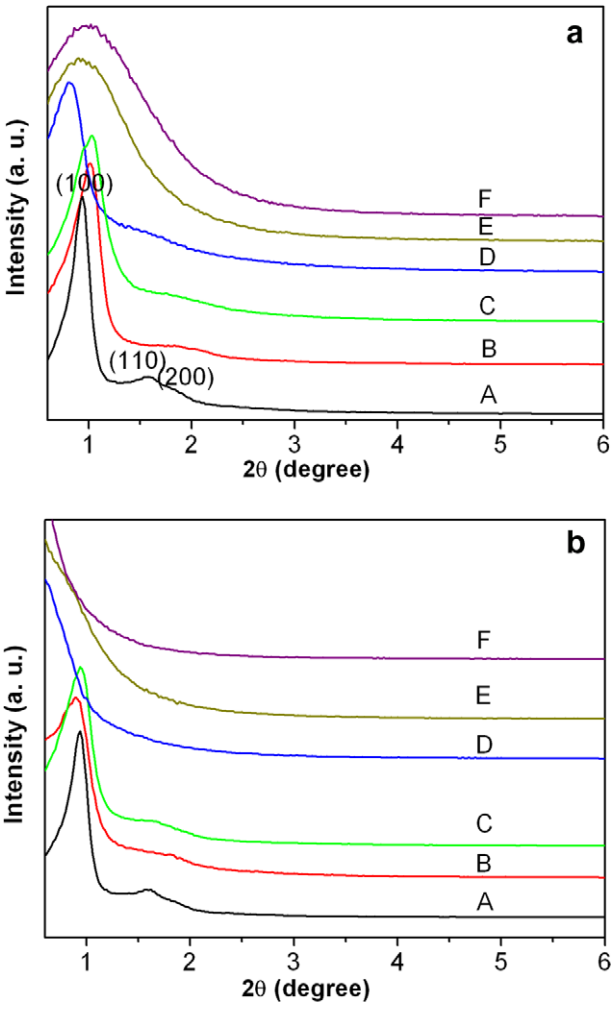

Fig. 6. Small-angle XRD patterns of ordered hexagonal mesostructured TiO_2–ZrO_2 composites with varied Ti/Zr ratios calcined at (a) 400 °C and (b) 600 °C. A: meso-10TZ, B: 20TZ, C: 40TZ, D: 60TZ, E: 80TZ, F: 90TZ.

are indexed to the combination of monoclinic and tetragonal phase of zirconia, while those of 40TZ and 60TZ exhibit a wide peak with a distinct diffraction peak at 2θ value of 30.2° which is indexed to the 101 diffraction peak of tetragonal phase. The wide-angle XRD pattern of mesoporous nanocomposite 80TZ and 90TZ samples calcined at 600 °C show typical diffraction peak of anatase phase. As the temperature increases to 600 °C, the diffractions especially for the 101 reflection at 2θ value of 25.4° become narrow and intense with particle size of 14 and 21 nm for 80TZ and 90TZ, respectively (calculated from Scherrer formula), indicating a further growth and a size increase of anatase nanocrystals, which results in the collapse of the mesostructure.

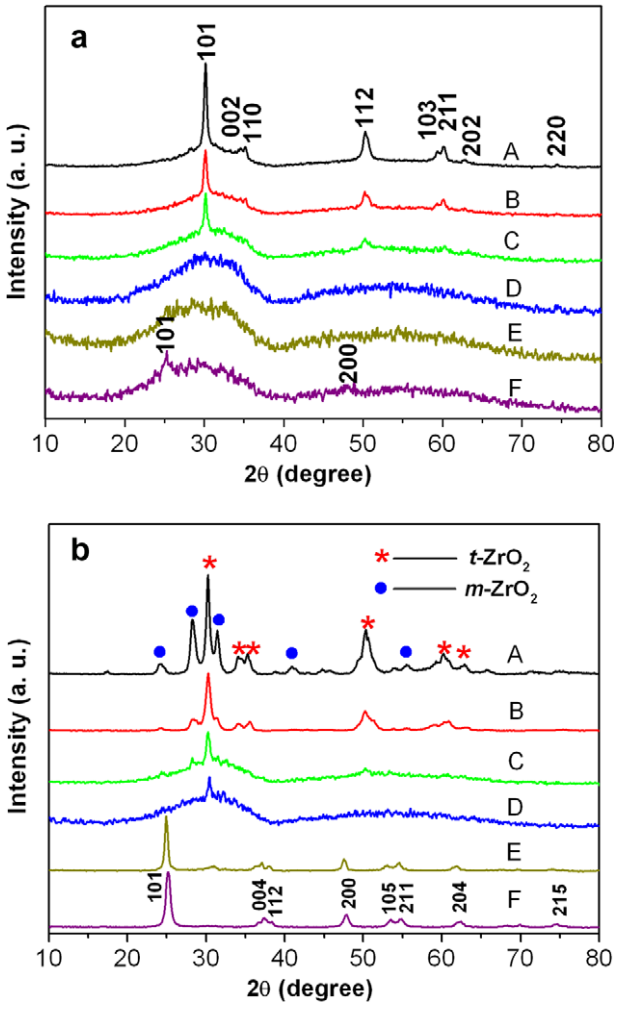

Fig. 7. Wide-angle XRD patterns of ordered hexagonal mesostructured TiO_2–ZrO_2 composites with varied Ti/Zr ratios calcined at (a) 400 °C and (b) 600 °C. A: meso-10TZ, B: 20TZ, C: 40TZ, D: 60TZ, E: 80TZ, F: 90TZ.

TEM images of mesoporous TiO_2–ZrO_2 composites with a variable Ti/Zr ratio are displayed in Fig. 8. The highly ordered hexagonal arrangement of pores along [0 0 1] direction and the alignment of cylindrical pores along [1 1 0] direction are observed in meso-20TZ (Fig. 8a), confirming the 2D hexagonal mesostructure. Similarly ordered mesoporous structures are also obtained in meso-40TZ and 60TZ (Fig. 8b and c). The cell parameters evaluated from TEM measurements are in the range of 8–11 nm, which are consistent with the *d* value calculated from the small-angle XRD patterns (Table 1). Fig. 8d shows the ordered channels in meso-20TZ calcined at 600 °C, further proving the ordered mesostructures are retained after 600 °C treatment.

Nitrogen adsorption–desorption isotherms of mesoporous TiO_2–ZrO_2 composites with different Ti/Zr ratios exhibit typical type IV curves with sharp capillary condensation steps between relative pressure (p/p_0) of 0.4–0.8, implying the well-uniform mesopores with very narrow pore size distribution (Fig. S2a and b in Supporting information). The hysteresis loops are very close to the H1 type, suggesting uniform cylindrical pore geometry. These mesoporous TiO_2–ZrO_2 composites possess BET specific surface areas as high as 90–250 $m^2\ g^{-1}$ (Table 1). It is mainly related to the mesostructual regularity resulted directly from the Ti/Zr ratio. The pore sizes calculated from the desorption data using the BJH model are in the range of 3.6–3.7 nm (Table 1), without obvious change when the Ti/Zr ratio varies. However, the pore size distribution curves broaden (Fig. S2b in Supporting information) with the increase of Ti/Zr ratio, indicating that the mesostructures are greatly degraded. The calculated pore wall thickness is in the range of 4.5–7.5 nm, which is in agreement with the TEM observations.

The heterogeneous photocatalytic degradation of RhB solution under UV light irradiation is detected with UV–vis spectrophotometer after adsorption–desorption equilibrium. The characteristic absorption bands of RhB located at 554 nm steadily decrease with increasing irradiation times and the representative photograph (Fig. 9) for the RhB solution using meso-50TZ calcined at 800 °C as catalyst clearly shows the decoloration process of RhB solutions along with irradiation time. Therefore, the concentration of RhB is evolved using the linear part of the absorbance–concentration curve (Beer's Law) and measuring absorbance to figure out the corresponding concentration. The photocatalytic activity of commercial nonporous photocatalyst P25 was also measured under the same condition for the purpose of comparison. Fig. 11a displays the time profiles of C/C_0 under UV light irradiation for meso-50TZ calcined at different temperatures, where C is the concentration of RhB at the irradiation time t and C_0 is the initial concentration. After light on, the concentration of RhB decreased with irradiation time and the pseudo-first-order reaction is observed. Samples calcined at 400, 800, and 900 °C all present good catalytic efficiency and the degradation process finished within 40 min, which is comparable with the commercial P25. Fig. 10a shows the time profiles of C/C_0 under UV light irradiation for the representative samples with different calcination temperatures. Similar to other studies on organic dyes, the degradation catalytic reactions is ascribed to a pseudo first-order reaction with a simplified Langmuir–Hinshelwood model when C_0 is very small [46–48]:

$$\ln(C_0/C) = kt$$

where k is the apparent first-order rate constant, as shown in Fig. 10b. The value of k gives an indication of the activity of the photocatalyst. The corresponding reaction rates for these three samples follow a trend TZ800 ($k = 0.086\ min^{-1}$) > TZ900 ($k = 0.077\ min^{-1}$) > TZ400 ($k = 0.066\ min^{-1}$). However, TZ600 shows slower decomposition rate and lower catalytic activities (Fig. 10a and b, $k = 0.039\ min^{-1}$). It is difficult to evaluate the effect of only one factor on photocatalytic activity excluding effects of other factors [49]. For example, crystallization of amorphous metal oxides by heat treatment resulted in simultaneous changes in other properties such as specific surface area, which is another main factor for reaction efficiency. It is presumed that the reaction rate is the results due to the combination of the specific surface area and crystallinity of the samples. Larger surface area provides more active sites and with no doubt the decomposition rate reduces when the surface area decreases. But here in our case, with the increase of calcination temperature, the crystallinity of the samples becomes better while the surface area decreases. In order to estimate the crystallinity on the decomposition behavior of our samples, the reaction rate k is divided by the surface area:

$$k_a = k/(m \cdot S_{BET})$$

where m is the mass of the sample and S_{BET} is the specific surface area of the sample, therefore, k_a is the decomposition rate per square meter. As shown in Fig. 10c, it is found that the decomposition rate per surface area follows the order of TZ900 ($k_a = 0.045\ min^{-1}\ m^{-2}$) > TZ800 ($k_a = 0.023\ min^{-1}\ m^{-2}$) > TZ400 ($k_a = 0.0035\ min^{-1}\ m^{-2}$) > TZ600 ($k_a = 0.0023\ min^{-1}\ m^{-2}$). This order obviously indicates that the reactivity becomes higher with the increase of sample crystallinity. Furthermore, representative samples with variable Ti/Zr ratios are also tested for degradation of RhB. The mesoporous composites of 20TZ ($k = 0.044\ min^{-1}$), 40TZ ($k = 0.065\ min^{-1}$), 60TZ ($k = 0.067\ min^{-1}$), and 80TZ ($k = 0.090\ min^{-1}$), exhibit photocatalytic activities (Fig. 10d and e) which are major related to

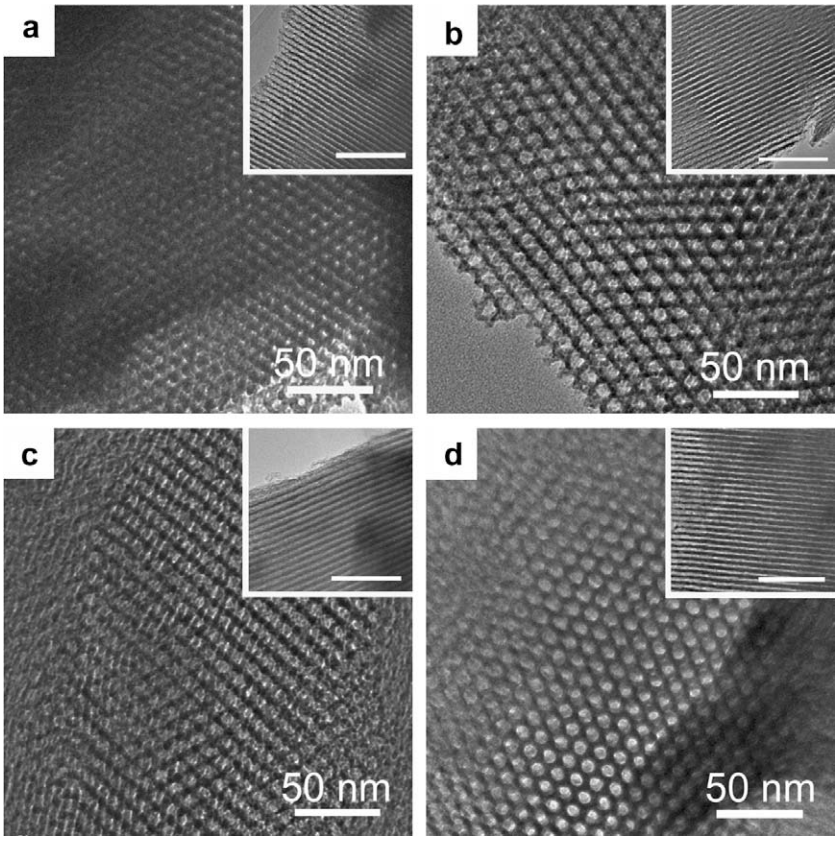

Fig. 8. TEM images of the mesostructured TiO_2–ZrO_2 composites with varied Ti/Zr ratios calcined at 400 °C: (a) meso-20TZ viewed along [0 0 1] orientation; (b) meso-40TZ viewed along [0 0 1] orientation; (c) meso-60TZ viewed along [0 0 1] orientation and (d) TEM images viewed along [0 0 1] orientation of the mesostructured 20TZ composites calcined at 600 °C. The insets are TEM images viewed along [1 1 0] orientation. The bars are 100 nm for insets.

Table 1
Physicochemical properties of the mesoporous TiO_2–ZrO_2 composites prepared with different Ti/Zr ratios and calcining temperatures.

Sample	Calcination temperature (°C)	BET surface area ($m^2\ g^{-1}$)	Pore size (nm)	Pore volume ($cm^3\ g^{-1}$)	d_{100} (nm)
meso-50TZ	400	186	4.6	0.29	9.0
	600	170	4.1	0.21	8.8
	800	37	–	0.23	–
	900	18	–	0.19	–
meso-10TZ	400	252	3.5	0.29	9.4
meso-20TZ	400	189	3.6	0.29	8.8
meso-40TZ	400	201	3.7	0.24	8.5
meso-60TZ	400	173	3.7	0.18	11.0
meso-80TZ	400	102	3.7	0.16	9.8
meso-90TZ	400	92	3.7	0.12	9.0

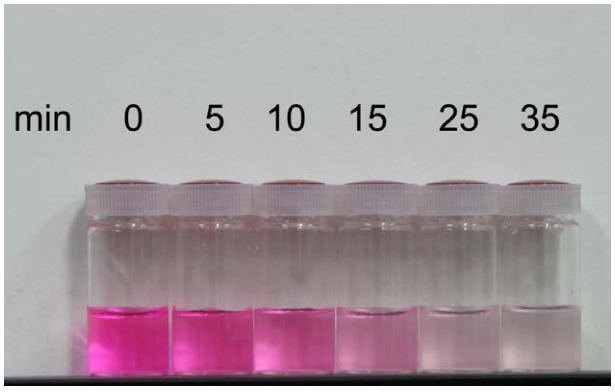

Fig. 9. The photo of RhB solution in the presence of TZ800 (0.1 g) at different time intervals (min) of (1) 0; (2) 5; (3) 10; (4) 15; (5) 25 and (6) 35, respectively.

the Ti/Zr ratio. To estimate the Ti/Zr ratio effect on the decomposition behavior of our samples, the reaction rate k is also divided by the surface area (Fig. 10f) as above. It is found that decomposition rate per surface area follows the order of 80TZ (k_a = 0.00882 - $min^{-1}\ m^{-2}$) > 60TZ (k_a = 0.00387 $min^{-1}\ m^{-2}$) > 40TZ (k_a = 0.00323 - $min^{-1}\ m^{-2}$) > 20TZ (k_a = 0.00233 $min^{-1}\ m^{-2}$). With an increase in the content of Ti, the degradation amount of RhB increases. This increase in activity is reasonable when the following points are taken into consideration: first, zirconia has a very large band gap, greater than 5 eV [50], so it cannot act as a photocatalyst under the irradiation conditions used for these experiments. Second, noticed from the wide-angle XRD data in Fig. 7, the crystallinity is found to be gradually improved with the increase of Ti. For comparison, commercial P25 with the same mass is also tested for degradation of RhB and exhibits a reaction rate of 0.044 min^{-1}. Most of our mesoporous TiO_2–ZrO_2 samples show higher photocatalytic activities than P25 except TZ600. Compared to P25, the Ti ratios of our

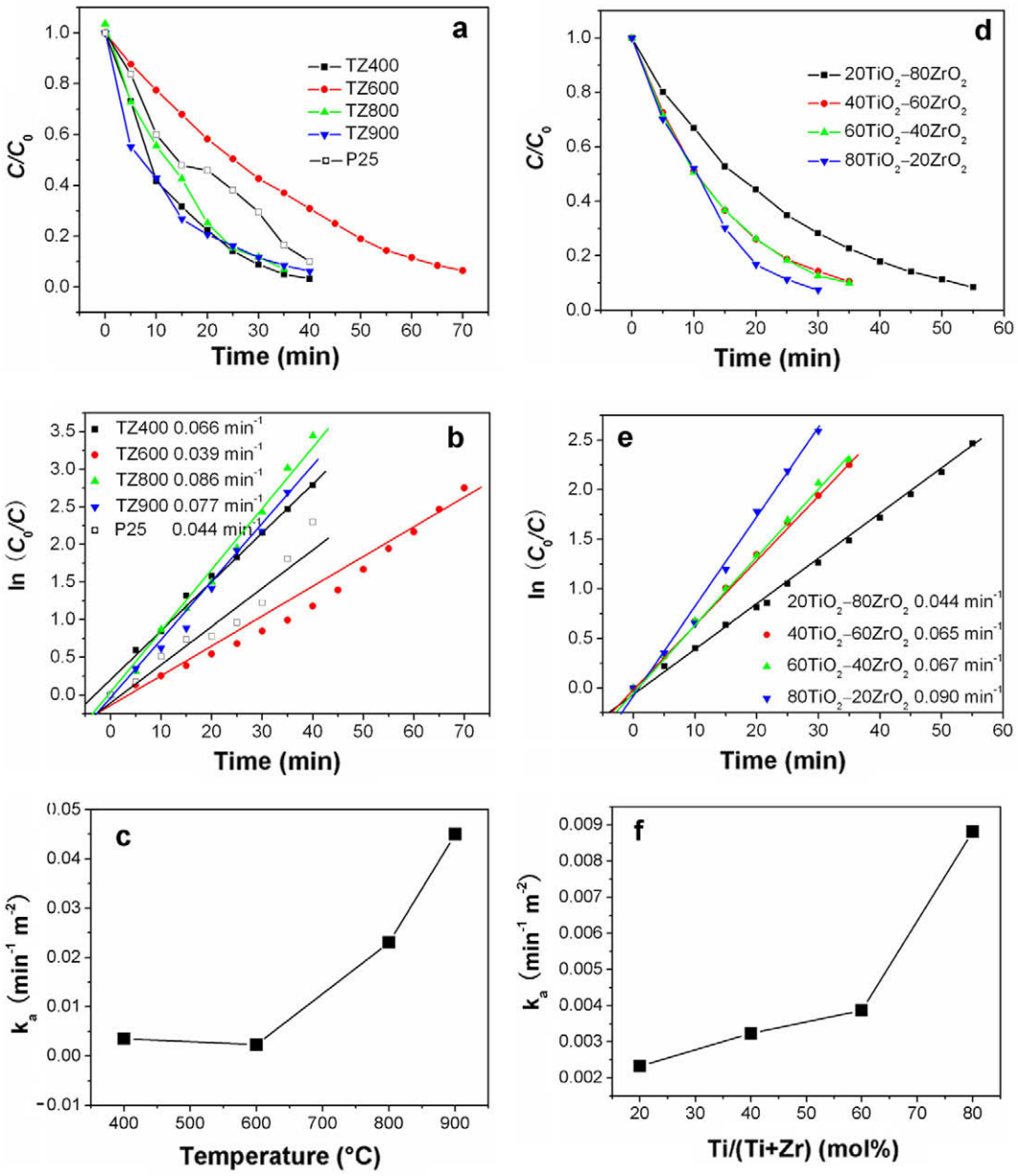

Fig. 10. Photocatalytic degradation of RhB monitored as the normalized concentration change versus irradiation time in the presence of (a) meso-50TZ calcined at different temperatures, (b) corresponding fit of RhB conversion data, and (c) corresponding reaction rate k_a (k divided by the surface area) versus calcination temperature; (d) concentration change versus irradiation time in the presence of mesoporous TiO_2–ZrO_2 with different Ti/Zr ratios, (e) corresponding fit of RhB conversion data, and (f) corresponding reaction rate k_a (k divided by the surface area) versus Ti content.

samples are lower, while the surface areas are larger. The sufficient amount of Zr inhibits remarkably crystallization and the consequent structural growth, resulting in high surface areas [18]. Large surface areas and pore volumes are beneficial to more RhB molecules absorbed in the channels to contact with active sites. The mesoporous TiO_2–ZrO_2 composites exhibit a binary function for the degradation of RhB derived from their crystalline of the framework and high surface areas [51].

The photocatalytic activity of the ordered mesoporous titania–zirconia composites for the hydrogen evolution reaction in methanol aqueous solution was investigated and a small amount of Pt, act as cocatalyst, was loaded onto the meso-50TZ surface by a photo deposition method using chloroplatinic acid as the Pt source. The chemical composition of the surface before and after Pt loading is provided by XPS (see Fig. S3 in Supporting information). The Ti 2p core level XPS spectrum has two peaks at 458.6 ($2p_{3/2}$) and 464.4 eV ($2p_{1/2}$) [52], and the spectra reveal no noticeable chemical valence change for Ti after Pt loading process. The formation of metallic Pt is confirmed by XPS analysis of the Pt/TiO_2–ZrO_2 surface. It shows two intense peaks centered at the binding energies of 72.9 and 76.2 eV. These two peaks are attributed to Pt $4f_{7/2}$ and Pt $4f_{5/2}$ excitation of metallic Pt, respectively [52]. Measured atomic concentrations, determined using XPS, of the Pt-loaded sample indicates the Pt/Ti ratio is about 0.3 mol% on the surface. All the samples are active photocatalysts for hydrogen evolution. Fig. 11a depicts the time dependent progress of photocatalytic reaction for the Pt loaded meso-50TZ samples calcined at different temperatures. The formation of H_2 commenced within ca. 15 min after the catalytic reactor containing suspension of Pt loaded meso-50TZ sample in water–methanol

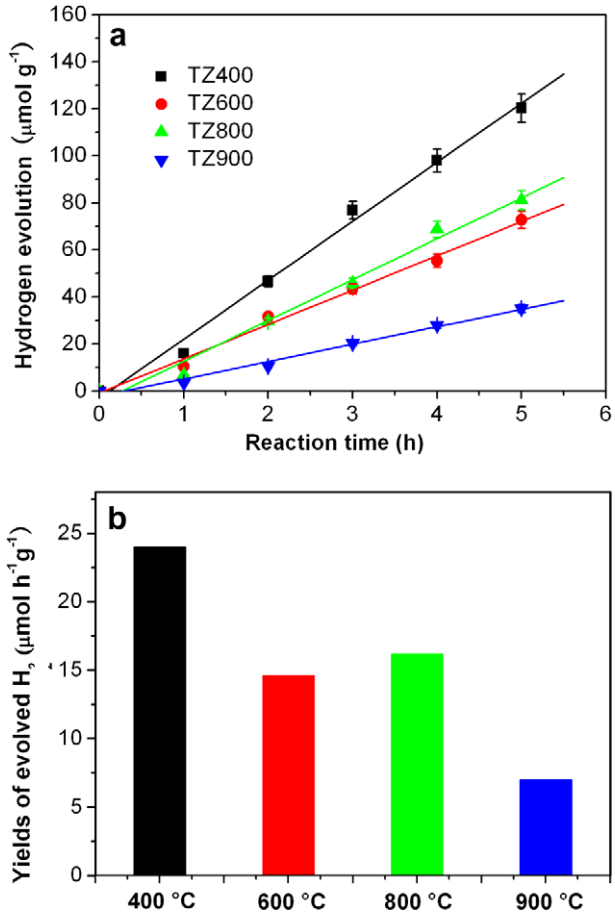

Fig. 11. (a) Overall water splitting over Pt-loaded meso-50TZ calcined at different temperatures under UV irradiation; (b) effect of calcinations temperature on the rate of gas evolution over Pt-loaded meso-50TZ.

mixture was exposed to UV light irradiation. No reaction was observed under dark condition. As seen in this figure, the meso-50TZ calcined at 400 °C (denoted as TZ400) exhibits a significant photocatalytic activity and the amount of hydrogen evolved per unit mass of sample decreases when the calcination temperature is raised to 600 °C. When the sample calcined at 800 °C (denoted as TZ800) is tested, for the beginning 2 h exposed to UV light irradiation, the yields of hydrogen are higher than that calcined at 600 °C (denoted as TZ600). This is the unique inflexion in the hydrogen evolution reaction for the meso-50TZ calcined at different temperatures. Whereas, when the reaction continues for longer than 2 h, the amount of hydrogen evolved becomes smaller than that of TZ600. The reaction rate (Fig. 11b) follows a trend: TZ400 > TZ800 > TZ600 > TZ900. The observation on the hydrogen evolution activity for these Pt loaded mesoporous TiO_2–ZrO_2 samples treated at different temperatures can be mainly attributed to the large surface area, porosity, and crystallinity of the samples [53]. First, the mesoporous TiO_2–ZrO_2 composites which possess differently effective activity sites provides different reaction sites for reactions. Second, the large surface area and through-porosity ensures the sufficient exposures to the UV light. Third, the different surface area and through-porosity allows different efficiencies for the adsorption of water molecules, thus changing their interaction with the photo-generated charge carriers. As mentioned above, the photocatalytic activity originates from photogenerated electron–hole pairs produced when it absorbs light with energy equal to or greater than that of its electronic band gap energy. Unfortunately, most photogenerated electrons and holes are consumed by volume and surface recombination [54] before they encounter adsorbed species. The recombination rate of photogenerated electron–hole pairs has been well proved to be highly dependent on the crystallite size, crystallinity, and morphology of photocatalysts. Therefore, it is presumed that another factor is that the large surface-to-volume ratio, porosity, and crystallinity of our samples result in an easier separation of electrons and holes.

4. Conclusions

A controlled synthesis of highly ordered mesoporous titania–zirconia composites with crystalline frameworks using tetrabutyl titanate and zirconium oxide chloride as titanium and zirconium sources, and triblock copolymer F127 and P123 as SDAs via an EISA process is demonstrated. The whole process is self-adjusting to organize the network-forming metal oxide species without extra acid or base. XRD, TEM, and nitrogen adsorption–desorption analysis techniques have been employed to systematically investigate the pore wall structure and thermal stability. The highly ordered mesoporous structures with 2D hexagonal symmetry are obtained by adjusting the amounts of SDAs under a proper relative humidity and evaporation temperature. A series of titania–zirconia nanocomposites with controlled texture properties and composition are obtained in a wide range from 10 to 90 mol% TiO_2 through tuning the initial mass ratios. The composites possess ordered 2D hexagonal mesostructure, high surface area (up to 200 $m^2\,g^{-1}$), large pore volume (0.1–0.3 $cm^3\,g^{-1}$), and uniform pore size (3.5–4.1 nm). The titania-zirconia composites show good photocatalytic activities for photodegradation of rhodamine B and hydrogen evolution in an aqueous suspension, which can be ascribed to the cooperative effect of the crystallinity and porosity of these materials. This approach may be developed to design more ordered mesoporous crystalline multi-metal composites with wide applications.

Acknowledgments

This work was supported by the MOST of China (2006CB601104), NSFC (20821091) and the Founder Foundation of PKU.

Appendix A. Supplementary data

EDX data of meso-50TZ (Fig. S1); Nitrogen adsorption–desorption isotherms and pore size distribution curves of mesostructured TiO_2–ZrO_2 composites with varied Ti/Zr ratios calcined at 400 °C (Fig. S2); XPS spectra of meso-50TZ (Fig. S3); band position and the number of Lewis acid sites of meso-50TZ (Table S1). Supplementary data associated with this article can be found, in the online version, at doi:10.1016/j.micromeso.2009.05.006.

References

[1] A. Hagfeldt, M. Grätzel, Chem. Rev. 95 (1995) 49.
[2] K. Rajeshwar, N.R. de Tacconi, C.R. Chenthamarakshan, Chem. Mater. 13 (2001) 2765.
[3] M. Kazuhiko, D. Kazunari, J. Phys. Chem. C 111 (2007) 7851.
[4] A. Fujishima, K. Honda, Nature 238 (1972) 37.
[5] A. Fujishima, K.B. Honda, Chem. Soc. Jpn. 44 (1971) 1148.
[6] K. Wilke, H.D. Breuer, J. Photochem. Photobiol. A: Chem. 121 (1999) 49.
[7] J.B. Miller, I.K. Edmond, Catal. Today 35 (1997) 269.
[8] J. Cai, C. Raptis, Y.S. Raptis, E. Anastassakis, Phys. Rev. B 51 (1995) 201.
[9] G. Morell, R.S. Kutiyar, D. Torres, S.E. Paje, J. Llopis, J. Appl. Phys. 81 (1997) 2830.
[10] K.M. Parida, S.K. Samantaray, H.K. Mishra, J. Colloid Interf. Sci. 216 (1999) 127.
[11] X. Gao, I.E. Wachs, Catal. Today 51 (1999) 233.

[12] S.K. Maity, M.S. Rana, S.K. Bej, J. Ancheyta-Juárez, G.M. Dhar, T.S.R.P. Rao, Catal. Lett. 72 (2001) 115.
[13] S.Y. Lai, W. Pan, C.F. Ng, Appl. Catal. B 24 (2000) 207.
[14] T. Klimova, E. Carmona, J. Ramirez, J. Mater. Sci. 33 (1998) 1981.
[15] J. Sekulic, A. Magraso, J.E. ten Elshof, D.H.A. Blank, Micropor. Mesopor. Mater. 72 (2004) 49.
[16] D. Das, H.K. Mishra, N.C. Pradhan, A.K. Dalai, K.M. Parida, Micropor. Mesopor. Mater. 80 (2005) 327.
[17] M.E. Zorn, D.T. Tompkins, W.A. Zeltner, M.A. Anderson, Appl. Catal. B 23 (1999) 1.
[18] J.H. Schattka, D.G. Shchukin, J.G. Jia, M. Antonietti, R.A. Caruso, Chem. Mater. 14 (2002) 5103.
[19] X. Fu, L.A. Clark, Q. Yang, M.A. Anderson, Environ. Sci. Technol. 30 (1996) 647.
[20] J.C. Yu, J. Lin, R.W.M. Kwok, J. Phys. Chem. B 102 (1998) 5094.
[21] T.S. Ahmadi, Z.L. Wang, T.C. Green, A. Henglein, M.A. El-Sayed, Science 272 (1996) 1924;
M. Bruchez, M. Moronne, P. Gin, S. Weiss, A.P. Alivisatos, Science 281 (1998) 2013;
Y. Sun, Y. Xia, Science 298 (2002) 2176;
Y.D. Yin, A.P. Alivisatos, Nature 437 (2005) 664.
[22] J.T. Hu, T.W. Odom, C.M. Lieber, Acc. Chem. Res. 32 (1999) 435.
[23] H.X. Mai, L.D. Sun, Y.W. Zhang, R. Si, W. Feng, H.P. Zhang, H.C. Liu, C.H. Yan, J. Phys. Chem. B 109 (2005) 24380.
[24] B.G. Trewyn, I.I. Slowing, S. Giri, H.T. Chen, V.S.-Y. Lin, Acc. Chem. Res. 40 (2007) 846.
[25] C.T. Kresge, M.E. Leonowicz, W.J. Roth, J.C. Vartul, J.S. Beck, Nature 359 (1992) 710;
J.S. Beck, J.C. Vartul, W.J. Roth, M.E. Leonowicz, C.T. Kresge, K.D. Schmitt, C.T.-W. Chu, D.H. Olson, E.W. Sheppard, S.B. McCullen, J.B. Higgins, J.L. Schlenkert, J. Am. Chem. Soc. 114 (1992) 10834.
[26] Q. Huo, D.I. Margolese, U. Ciesla, P. Feng, T.E. Gier, P. Sieger, R. Leon, P.M. Petroff, F. Schüth, G.D. Stucky, Nature 368 (1994) 317;
D.M. Antonelli, A. Nakahira, J.Y. Ying, Inorg. Chem. 35 (1996) 3126;
P. Yang, D. Zhao, D.I. Margolese, B.F. Chmelka, G.D. Stucky, Nature 396 (1998) 152;
E.L. Crepaldi, G.J. De, A.A. Soler-Illia, D. Grosso, F. Cagnol, F. Ribot, C. Sanchez, J. Am. Chem. Soc. 125 (2003) 9770;
X. Xu, B. Tian, J. Kong, S. Zhang, B. Liu, D. Zhao, Adv. Mater. 15 (2003) 1932;
B. Tian, X. Liu, L.A. Solovyov, Z. Liu, H. Yang, Z. Zhang, S. Xie, F. Zhang, B. Tu, C. Yu, O. Terasaki, D. Zhao, J. Am. Chem. Soc. 126 (2004) 865;
A.K. Sinha, K. Suzuki, Angew. Chem. Int. Ed. 44 (2005) 271;
H. Shibata, T. Ogura, T. Mukai, T. Ohkubo, H. Sakai, M. Abe, J. Am. Chem. Soc. 127 (2005) 16396;
Y. Wang, C.M. Yang, W. Schmidt, B. Spliethoff, E. Bill, F. Schüth, Adv. Mater. 17 (2005) 53;
F. Jiao, A. Harrison, J.C. Jumas, A.V. Chadwick, W. Kockelmann, P.G. Bruce, J. Am. Chem. Soc. 128 (2006) 5468;
X. Lai, X. Li, W. Geng, J. Tu, J. Li, S. Qiu, Angew. Chem. Int. Ed. 46 (2007) 738;
Y. Shi, Y. Wan, R. Liu, B. Tu, D. Zhao, J. Am. Chem. Soc. 129 (2007) 9522.
[27] C.J. Brinker, Y. Lu, A. Sellinger, H. Fan, Adv. Mater. 11 (1999) 579.
[28] Y. Lu, H. Fan, A. Stump, T.L. Ward, T. Rieker, C.J. Brinker, Nature 398 (1999) 223.
[29] P.D. Yang, D.Y. Zhao, D.I. Margolese, B.F. Chmelka, G.D. Stucky, Nature 396 (1998) 152;
P.D. Yang, D.Y. Zhao, D.I. Margolese, B.F. Chmelka, G.D. Stucky, Chem. Mater. 11 (1999) 2813.
[30] H.S. Yun, K. Miyazawa, H.S. Zhou, I. Honma, M. Kuwabara, Adv. Mater. 13 (2001) 1377.
[31] F. Schüth, Chem. Mater. 13 (2001) 3184.
[32] K. Cassiers, T. Linssen, V. Meynen, P. Van der Voort, P. Cool, E.F. Vansant, Chem. Commun. (2003) 1178.
[33] K.X. Wang, M.A. Morris, J.D. Holmes, Chem. Mater. 17 (2005) 1269.
[34] D. Grosso, G. Soler-Illia, E.L. Crepaldi, F. Cagnol, C. Sinturel, A. Bourgeois, A. Brunet-Bruneau, H. Amenitsch, P.A. Albouy, C. Sanchez, Chem. Mater. 15 (2003) 4562.
[35] H. Choi, A.C. Sofranko, D.D. Dionysiou, Adv. Funct. Mater. 16 (2006) 1067.
[36] S.Y. Choi, M. Mamak, N. Coombs, N. Chopra, G.A. Ozin, Adv. Funct. Mater. 14 (2004) 335.
[37] B. Smarsly, D. Grosso, T. Brezesinski, N. Pinna, C. Boissiere, M. Antonietti, C. Sanchez, Chem. Mater. 16 (2004) 2948.
[38] D. Grosso, C. Boissière, B. Smarsly, T. Brezesinski, N. Pinna, P.A. Albouy, H. Amenitsch, M. Antonietti, C. Sanchez, Nat. Mater. 3 (2004) 787.
[39] M. Zorn, D.T. Tompkins, W.A. Zeltner, M.A. Anderson, Environ. Sci. Technol. 34 (2000) 5206.
[40] S.W. Liu, Z.L. Xiu, J. Pan, X.P. Cui, W.N. Yu, J.X. Yu, J. Alloys Compd. 437 (2007) L1.
[41] R.A. Lucky, P.A. Charpentier, Adv. Mater. 20 (2008) 1755.
[42] W. Zhou, K.S. Liu, H.G. Fu, K. Pan, L.L. Zhang, L. Wang, C.-C. Sun, Nanotechnology 19 (2008) 035610.
[43] G. Parfitt, J. Ramsbotham, C. Rochester, Trans. Faraday Soc. 581 (1971) 1500.
[44] A. Firouzi, D. Kumar, L.M. Bull, T. Besier, P. Sieger, Q. Huo, S.A. Walke, J.A. Zasadzinski, C. Glinka, J. Nicol, D. Margolese, G.D. Stucky, B.F. Chmelka, Science 267 (1995) 1138.
[45] G.J.A.A. Soler-Illia, C. Sanchez, B. Lebeau, J. Patarin, Chem. Rev. 102 (2002) 4093.
[46] X.H. Wang, J.G. Li, H. Kamiyama, Y. Moriyoshi, T. Ishigaki, J. Phys. Chem. B 110 (2006) 6804.
[47] Y. Yu, J.C. Yu, C.Y. Chan, Y.K. Che, J.C. Zhao, L. Ding, W.K. Ge, P.K. Wong, Appl. Catal. B 61 (2005) 1.
[48] J. Li, H.C. Zeng, Chem. Mater. 18 (2006) 4270;
A. Houas, H. Lachheb, M. Ksibi, E. Elaloui, C. Guillard, J. Herrmann, Appl. Catal. B 31 (2001) 145.
[49] B. Ohtani, Y. Ogawa, S. Nishimoto, J. Phys. Chem. B 101 (1997) 3746.
[50] S.M. Chang, R.A. Doong, J. Phys. Chem. B 108 (2004) 18098.
[51] W.Y. Dong, Y.J. Sun, C.W. Lee, W.M. Hua, X.C. Lu, Y.F. Shi, S.C. Zhang, J.M. Chen, D.Y. Zhao, J. Am. Chem. Soc. 129 (2007) 13894.
[52] J. Chastain (Ed.), Handbook of X-ray Photoelectron Spectroscopy, Perkin-Elmer Corporation, Eden Prairie, MN, 1992.
[53] (a) F.E. Osterloh, Chem. Mater. 20 (2008) 35;
(b) P.S. Lunawat, R. Kumar, N.M. Gupta, Catal. Lett. 121 (2008) 226.
[54] S.P.S. Badwal, Appl. Phys. A 50 (1990) 449.